

Effect of structure and orientation of incident carbon-cluster ions C_n^+ ($n \leq 4$) on secondary-ion emission induced by electronic excitation

Ryu Murase,^{1,*} Hidetsugu Tsuchida^{1,2,†} Sohei Nakagawa,¹ Shigeo Tomita^{1,3} Atsuya Chiba,⁴ Kaoru Nakajima,⁵ Takuya Majima¹ and Manabu Saito^{1,2}

¹Department of Nuclear Engineering, Kyoto University, Kyoto 615-8530, Japan

²Quantum Science and Engineering Center, Kyoto University, Uji, Kyoto 611-0011, Japan

³Institute of Applied Physics, University of Tsukuba, Tsukuba, Ibaraki 305-8573, Japan

⁴Takasaki Advanced Radiation Research Institute, National Institutes for Quantum and Radiological Science and Technology, Takasaki, Gunma 370-1292, Japan

⁵Department of Micro Engineering, Kyoto University, Kyoto 615-8530, Japan



(Received 25 March 2021; accepted 8 June 2021; published 28 June 2021)

We present experimental results that show the secondary-ion yield depends on the structure and orientation of incident cluster ions. A beam of carbon-cluster ions C_n^+ ($n \leq 4$) with an energy of 0.9 MeV per atom, which were obtained from a tandem electrostatic accelerator, was incident on a glycine target deposited on a carbon foil. The structure and orientation of the cluster ions after passing through the target were determined by the Coulomb explosion imaging method, and the positive secondary ions were simultaneously measured by time-of-flight mass spectrometry. When looking at the orientation dependence of linear structured C_2^+ , C_3^+ , and C_4^+ projectiles, parallel orientations with respect to the beam direction were found to enhance the secondary-ion yield compared with perpendicular orientations. Additionally, comparison of the structure dependence of C_3^+ and C_4^+ projectiles with linear and ring structures showed that the secondary-ion yield was larger for linear structures. Interestingly, there was a clear correlation between the secondary-ion yield and the deposited energy density in the cluster-ion track. The energy density was calculated with electronic stopping power for incident cluster ions using linear-response dielectric theory and the cross section of the track of the incident cluster considering its geometrical structure and orientation. These results suggest that the deposited energy density in the cluster-ion track is a key parameter in the secondary-ion emission process induced by swift cluster-ion impacts.

DOI: [10.1103/PhysRevA.103.062812](https://doi.org/10.1103/PhysRevA.103.062812)

I. INTRODUCTION

Swift cluster-ion beams can uniquely impart large quantities of energy to the electronic system of a substance. This transfer results from the interference effect between the constituent atoms of a cluster, which is termed the vicinage effect. The magnitude of the vicinage effect varies depending on the number of cluster atoms n and acts on collisional interaction processes (energy loss of cluster ions [1–4]) and irradiation effects on the surface (secondary electron emission [5–7], sputtering [8–10], and surface modifications [11]). Many experimental and theoretical studies have been devoted to understanding the cluster size dependence of the energy-loss process. Experiments by Tomita *et al.* [1] have shown that the energy loss of C_n^+ ($n \leq 4$) with an energy of 0.5 MeV per atom in thin carbon foil is larger than that of monoatomic ions at the same velocity, but when compared in terms of energy loss per atom, it is smaller for cluster ions. This is attributed to the charge state of the constituent atoms of cluster [12]. Brunelle *et al.* [13] measured the charge state of atomic particles formed by decomposition of incident clusters of C_n^+

($n = 3–10$) in foil penetration, and found that the average charge of the decomposed atomic particles decreased with increasing cluster size and was smaller than the equilibrium charge of monoatomic C_1^+ passed through carbon foil. Chiba *et al.* [14] investigated the relationship between the structure of cluster projectiles and the average charge of decomposed atomic particles for foil penetration of 3 MeV C_3^+ with linear and triangular structures using a Coulomb explosion imaging method, and found that the average charge was larger for linear clusters. Additionally, when comparing the charges of each of three linearly arranged particles, the charge of the central particle was smaller than that of the particles at both ends. In this way, the vicinage effect is a phenomenon in which the constituent atoms of a cluster interfere with each other and interact with matter.

The vicinage effect depends both on the cluster structure and its orientation. According to calculations by Heredia-Avalos and Garcia-Molina [2], diatomic molecules (N_2^+) oriented parallel to the beam direction have lower energy loss than randomly oriented molecules. This calculation agrees well with the experiments reported by Steuer *et al.* [15]. Kaneko [3] calculated the energy loss for linear-structured C_n^+ ($n \leq 4$) with an energy of 0.5 MeV per atom passing through carbon foil and found that the energy loss was lower for parallel orientations than perpendicular orientations. They

*murase.ryu.86c@kyoto-u.jp

†tsuchida@nucleng.kyoto-u.ac.jp

also investigated the effect of cluster structure on the energy loss of C_n^+ ($n = 2-10$) over a wide range of velocities (1–10 a.u.). The results suggested that the energy loss of C_n^+ ($n \leq 4$) differed between linear and ring structures, and this difference depended on the projectile velocity [16].

As described above, because the incident cluster orientation affects energy deposition to matter, it is expected to affect various irradiation effects such as secondary particle emission from the surface. Some studies have been conducted on the influence of cluster orientation on the emission of secondary electrons and ions. Azuma *et al.* [7] measured the number of secondary electrons emitted from thin carbon foil both in the forward and backward directions from the passage of 8 MeV He_2^+ . They found that He_2^+ with a parallel orientation produced more secondary electrons than that with a perpendicular orientation in the forward emission, while there was no remarkable orientation effect observed in backward emission. In a previous study [10], we measured the secondary-ion yield emitted to the forward direction from phenylalanine foil induced by 3.6 MeV C_2^+ impacts and demonstrated that the secondary-ion yield for parallel orientations was approximately 1.1 times that for perpendicular orientations.

In the present work, we investigate the effect of the incident cluster structure on secondary-ion emission processes. We used cluster projectiles of C_n^+ ($n \leq 4$) with an energy of 0.9 MeV per atom. These carbon-cluster ions have a variety of geometric structures depending on the cluster size n . For instance, C_n^+ ($n \geq 3$) can have linear, triangular, or ring structures [14,17–23]. We performed coincidence measurements between the geometric structural analysis of incident clusters by the Coulomb explosion imaging method and the identification of positive secondary ions by time-of-flight mass spectrometry. For these measurements, we used a self-supported foil target consisting of glycine (Gly) deposited on a thin carbon foil. We employed Gly as the target because it has simple molecular structure and has been widely used in studies of the ion-induced secondary-ion emission process [24–26]. We investigate changes in the yields of Gly-related secondary ions with respect to the structure and orientation of the incident cluster. We discuss the relationship between the secondary-ion yield and the energy density deposited in the ion tracks of cluster projectiles.

II. METHODS

A. Experiments

The experiments were performed using a 2-MV tandem Pelletron accelerator (6SDH-2, National Electrostatics Corp., Middleton, Wisconsin) at the Quantum Science and Engineering Center of Kyoto University. The experimental setup (Fig. 1) was essentially the same as that used in our previous study [10]. To generate a swift cluster-ion beam, negatively charged cluster ions produced by Cs sputtering of a negative ion source were incident on a tandem accelerator and accelerated to a positive potential terminal in the center of the accelerator. When the accelerated negative cluster ions collided with the stripper gas (N_2) in the terminal, they become positive ions and were accelerated again. After analyzing the energy with a switching magnet, the desired positive cluster

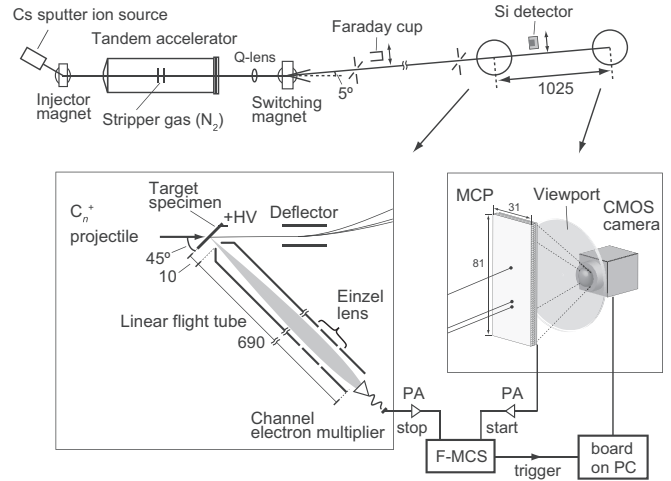


FIG. 1. Schematic of the experimental setup.

ions were guided to the beamline. The deflection angle of this beamline was 5° with respect to the accelerator tube.

Projectile beams were C_n^+ ($n \leq 4$) with an energy of 0.9 MeV per atom. The corresponding projectile velocity was $v = 1.73$ a.u., and electronic excitation predominated in interaction with matter. The beam was carefully collimated to a divergence angle of less than 0.5 mrad and a spot size of 0.1×0.1 mm² by two sets of four-jaw slits. To avoid dissociation of the incident cluster ions caused by residual gas collisions, the base pressure of the beamline and experimental chamber was kept below 2×10^{-5} Pa during the experiments. The measured fraction of the dissociated beam component was below 1%, which was confirmed by measuring the beam energy with a silicon semiconductor detector behind the target.

The target specimen was composed of glycine (99% purity, Nacalai Tesque, Inc., Japan) evaporated on carbon foil with a thickness of $1.0 \mu\text{g cm}^{-2}$ (The Arizona Carbon Foil Co., Inc., United States). A projectile of C_n^+ ($n \leq 4$) entered at the front of the target (carbon foil) with an incidence angle of 45° and then collided with a glycine layer prepared on the back surface of the target. The glycine layer was prepared under vacuum at $2-4 \times 10^{-4}$ Pa by the vacuum evaporation method with a maximum evaporation temperature (519 K) lower than the thermal decomposition temperature of Gly (523 K) [27]. In this case, the evaporation temperature was close to the thermal decomposition temperature of Gly, so there is no guarantee that Gly did not decompose. Assuming isotropic evaporation, the thickness t of the deposited Gly film is given by $t = m / (2\pi d^2 \rho_{\text{Gly}})$, where d is the distance between the carbon foil and the evaporation source ($d = 240$ mm), m is the weight of the Gly powder evaporated ($m = 3.6$ mg), and ρ_{Gly} is the density of Gly ($\rho_{\text{Gly}} = 1.16$ g cm⁻³). The estimated thickness of the Gly film was approximately 8 nm.

When the incident cluster ions passed through the foil, the C_n^+ fragmented into atomic C^{q+} with a charge state q and was separated by Coulomb repulsion. The outgoing C^{q+} ions were deflected according to the charge q with an electric field applied by a parallel plate deflector in the vertical direction and then hit a microchannel plate (MCP) detector with

a phosphor screen anode. The MCP was located 1025 mm downstream from the target. This is called the foil-induced Coulomb explosion imaging method, and it enables determination of the cluster structure and orientation [28]. The MCP had an effective detection area of $31 \times 81 \text{ mm}^2$ and an open area ratio of 60% (F2813-22P, Hamamatsu Photonics K.K., Japan). A two-dimensional image of the outgoing atomic fragments was recorded with a complementary metal-oxide semiconductor (CMOS) camera (EoSens MC1362, Mikrotron GmbH, Germany) from the outside of a vacuum chamber through a view port. A shutter trigger for the CMOS camera was provided by the MCP signal through a multichannel scaler. The shutter speed was set at 2 ms because the decay time of the luminescence from the phosphor screen was 1 ms. Meanwhile, positive secondary ions emitted from the Gly layer were accelerated by a target potential biased at +3.50 kV and detected by a channel electron multiplier (4869, Photonis, United States) after traveling through a linear flight tube (length: 690 mm) equipped with an einzel lens. The applied voltage of the einzel lens was 2.05 kV, which was chosen to achieve the highest mass resolution. The fluence of incident carbon-cluster projectiles was set below 10^{12} carbon particles cm^{-2} for one irradiation spot, which corresponds to the fluence to minimize the interaction of primary beams to the top monolayer of molecules in static secondary-ion mass spectrometry [29].

We performed coincidence measurements of time-of-flight (TOF) mass spectra between signals of the transmitted fragments (start trigger) and secondary ions (stop trigger) with a multiple-event fast multichannel scaler (F-MCS: MCS6A, FAST ComTec GmbH, Germany). The detection signals of the MCP and the channel electron multiplier were processed with fast preamplifiers and constant fraction discriminators. Timing output signals from the constant fraction discriminators were entered into the F-MCS as start and stop signals, and the time difference between both signals was measured as the flight time of secondary ions. When a start signal from the MCP was detected, a trigger signal for the CMOS camera was sent from the F-MCS to a frame grabber board (PCIe1473R, National Instruments Corp., United States) controlling the CMOS camera. After that, image acquisition started. The coordinate data of luminescent points on the phosphor screen anode were obtained by on-board processing of the acquired images and stored in a PC. To avoid accumulation of the luminescent signals from the phosphor screen anode, the count rate of the MCP was kept below 200 cps. The threshold level of the luminescent signals was set to 10% relative to the pulse height of the maximum luminescence intensity, and the background level was below 10%. Data for the position of outgoing fragments and the secondary-ion flight times were stored in an event-by-event mode.

B. Determination of the structure and orientation of incident cluster ions

We identified the structure and orientation of cluster projectiles C_n^+ ($n \leq 4$) from Coulomb explosion imaging data. In this study, orientation angles of 0° – 30° and 60° – 90° with respect to the beam direction were defined as parallel and perpendicular orientations, respectively. The C_2^+ projectiles

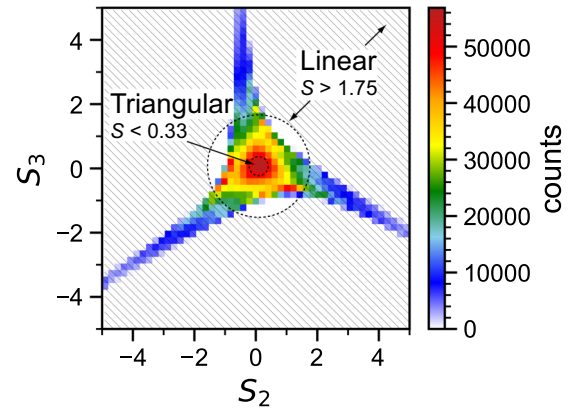


FIG. 2. Distribution of symmetric coordinates used for determination of the C_3^+ structure.

had various orientation angles to the beam direction. The orientation angles were determined from calculations using the Coulomb explosion model [10]. The C_3^+ projectiles had linear and triangular structures [18–21]. In the determination of the C_3^+ structure, we applied the following symmetric coordinates that were used to determine the C_3 cluster [14,30,31]:

$$S_2 = \frac{D_{12} - D_{23}}{\sqrt{2}}, \quad S_3 = \frac{2D_{31} - D_{23} - D_{12}}{\sqrt{6}}, \quad (1)$$

$$D_{ij} = \frac{d_i}{d_j}, \quad (2)$$

where d_i is the distance from the center of mass in the two-dimensional image pattern for the i th detection point. All possible permutations of i and j were included. Figure 2 shows the measured distribution under symmetric coordinates for all detection patterns. In this coordinate, the origin ($S_2 = S_3 = 0$) corresponds to an equilateral triangle pattern, and points well separated from the origin correspond to linear patterns. Using the relationship of $S = \sqrt{S_2^2 + S_3^2}$, we distinguished linear and triangular patterns by the distance from the origin; that is, patterns for $S < 0.33$ and $S > 1.75$ were considered to be triangular and linear structures, respectively. This relationship gave accuracies of 73% and 97% for ring and linear structure, respectively [30]. For linear patterns, we also obtained orientation angles from a distance between the detected points of two edge-positioned fragments. The orientation angle was calculated using the Coulomb explosion model considering the charge state of each atomic fragment. The C_4^+ projectiles had linear and ring structures [22,23]. To determine the structures from patterns, which consisted of four detection points, we used the following criterion. First, we obtained the distance l between the two most distant points, which were denoted as P1 and P4. Then we calculated the distances d_2 and d_3 , which were the distances from the remaining two points (P2 and P3) to the line connecting P1 and P4. We treated the patterns that satisfied $d_2/l < 0.15$ and $d_3/l < 0.15$ as linear structures and the patterns that satisfied $d_2/l > 0.40$ and $d_3/l > 0.40$ as ring structures. For linear patterns, we also obtained the orientation angle using the Coulomb explosion calculation.

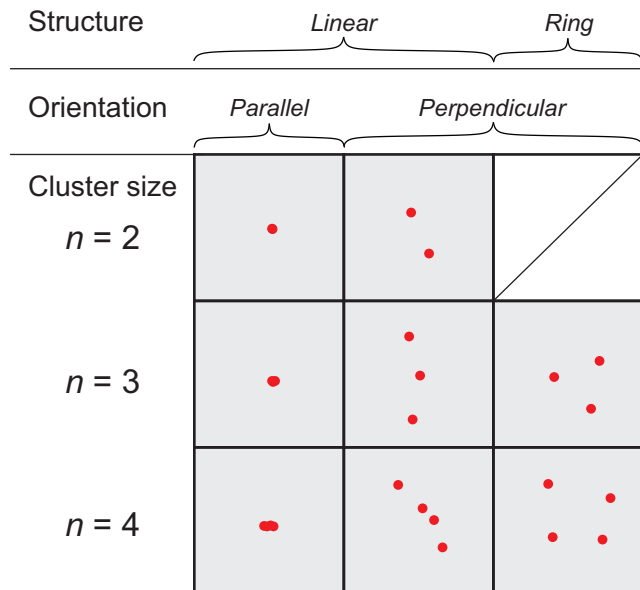


FIG. 3. Two-dimensional image of the fragmentation pattern for foil-induced Coulomb explosion of cluster projectiles C_n^+ ($n = 2-4$).

III. RESULTS

Figure 3 shows examples of the dissociated ion detection patterns in foil-induced Coulomb explosion imaging of cluster projectiles C_n^+ with $n = 2-4$. The results are shown according to the combination of structure and orientation for clusters with different n . In the left column, the image pattern consists of almost a single spot, which indicates that the C_n^+ clusters have a linear structure and parallel orientation. In this case, the lateral momentum of the dissociated ions gained by Coulomb explosion is nearly zero because C_n^+ are oriented parallel to the beam direction. The right column shows a pattern of triangles and rectangles for C_3^+ and C_4^+ projectiles, respectively, with perpendicular orientation. It should be noted that ring-structured clusters with a cluster plane parallel to the beam direction could not be distinguished from linear clusters in this measurement because we did not measure the parallel component of the momenta with respect to the beam direction.

Figure 4 shows a TOF mass spectrum of positive secondary ions from Gly bombarded by C_n^+ ($n \leq 4$) with an energy of 0.9 MeV per atom. The lower and upper abscissas denote the TOF channels and the corresponding mass-to-charge ratio, respectively. The vertical axis denotes the secondary-ion counts normalized with the number of incident clusters. The mass spectra for different structures and orientations of C_n^+ clusters with $n = 2, 3$, and 4 are shown by different lines. The spectral pattern was the same regardless of the value of n . Observed peaks correspond to Gly-related species and other species that do not originate from Gly. The former are protonated intact ions of GlyH^+ ($m/z = 76$), methylene amine cations (CH_4N^+ , $m/z = 30$) originating from the cleavage of a C-C $_{\alpha}$ bond, and ammonium cations (NH_4^+ , $m/z = 18$). The latter are hydrogen ions (H^+) and their molecules H_2^+ and H_3^+ , sodium cations (Na^+), and hydrocarbon cations. For the hydrocarbons, cations consisting of two carbons (C_2H_x^+ , $m/z = 26-31$), three carbons (C_3H_x^+ , $m/z = 38-45$), and

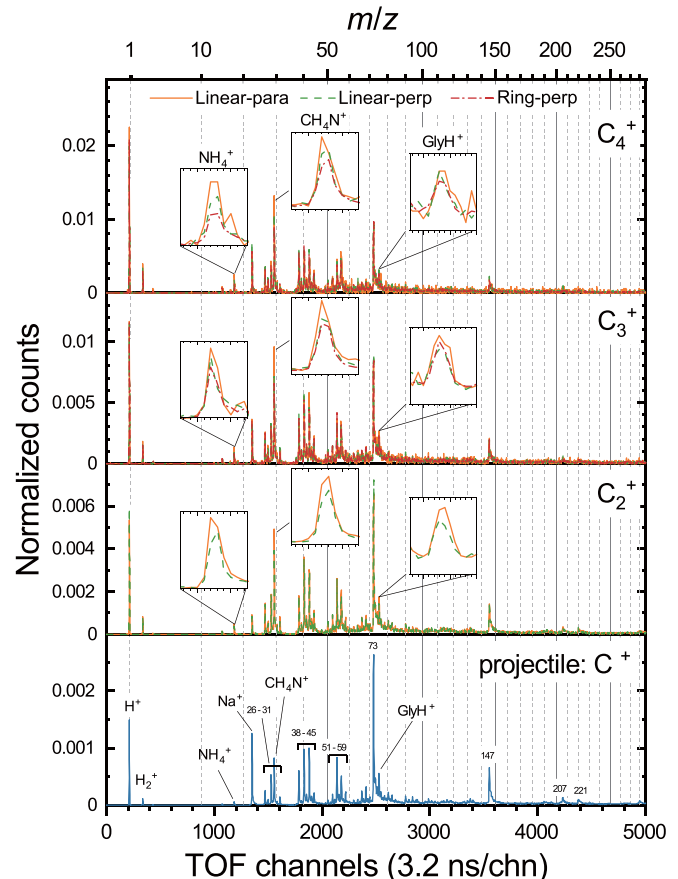


FIG. 4. Time-of-flight mass spectra of positive secondary ions emitted to the forward direction from a glycine target foil with C_n^+ ($n \leq 4$) impact. In the lower abscissa, the channel number of the multichannel scaler is 3.2 ns per channel. The upper abscissa denotes the mass-to-charge ratio of secondary ions. Insets show enlargements of the peaks for the Gly-related secondary ions GlyH^+ , CH_4N^+ , and NH_4^+ . For C_n^+ projectiles with $n = 2-4$, the spectra for different structures and orientations are indicated by different colored lines as follows: solid orange lines, linear and parallel; dashed green lines, linear and perpendicular; and dash-dotted red lines, ring and perpendicular.

four carbons (C_4H_x^+ , $m/z = 51-59$) were observed as a series of peaks. The peaks with $m/z = 73, 147, 207$, and 221 corresponded to polydimethylsiloxane, which is used as an industrial material [32]. The Na^+ , hydrocarbon cations, and polydimethylsiloxane-related cations may originate from contaminants on the target surface introduced during sample preparation or preservation because they are not observed in other mass spectroscopic studies for Gly [24–26].

We focused on the effects of the incident cluster structure and orientation on the formation of the Gly-related ion species GlyH^+ , CH_4N^+ , and NH_4^+ , which are typical ion species observed in secondary-ion mass spectrometry for the Gly target [26]. The insets in Fig. 4 are enlarged views of the peaks for these species. Interestingly, their peak intensities were clearly different for all cluster projectiles and depended on the cluster orientation and structure. Additionally, for cluster projectiles with a linear structure and parallel orientation, the mass spectrum peak intensity seemed to be high compared

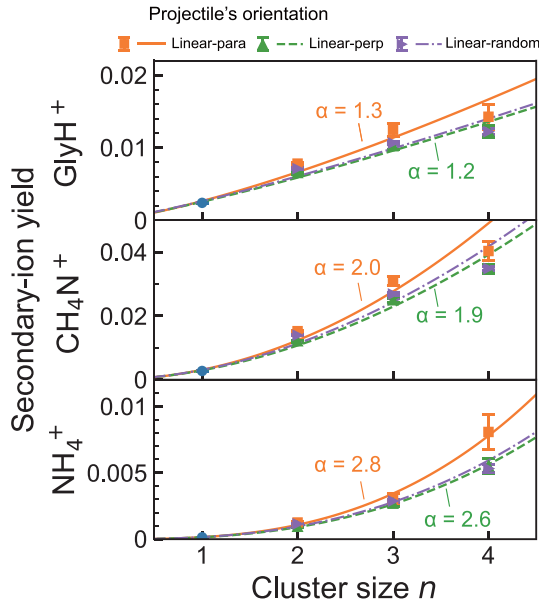


FIG. 5. Comparison of secondary-ion yields for the Gly-related species GlyH^+ , CH_4N^+ , and NH_4^+ induced by linear cluster projectiles with parallel, perpendicular, and random orientations. The vertical scale denotes the yield normalized with the number of incident clusters. The lines indicate the power-law distribution obtained by fitting the data for each orientation. The value of α is the exponent for parallel and perpendicular orientations.

with that for cluster projectiles with a linear or ring structure and perpendicular orientation.

To evaluate these trends in detail, we obtained the secondary-ion yield by integrating the peak for each Gly-related ion species. Figure 5 displays the ion yields of GlyH^+ , CH_4N^+ , and NH_4^+ for each geometrical characteristic of the cluster projectiles with a linear structure, including the size and orientation. Each symbol denotes the results for parallel, perpendicular, and random orientation. Random includes all orientations of linear-structured projectiles. The ion yield increased with increasing n , and the n dependence exhibited nonlinear behavior for every secondary-ion species. It is well known that the ion yield follows a power-law distribution n^α , where $\alpha > 1$ [33]. By fitting the data with a power-law distribution, $Y \propto n^\alpha$, we obtained the exponent α . For GlyH^+ , CH_4N^+ , and NH_4^+ in parallel orientations, the values of α were 1.3 ± 0.2 , 2.0 ± 0.2 , and 2.8 ± 0.1 , respectively. In perpendicular orientations, the values of α for GlyH^+ , CH_4N^+ , and NH_4^+ were 1.2 ± 0.1 , 1.9 ± 0.1 , and 2.6 ± 0.1 , respectively. Thus, the value of α depends on the orientation and is larger for parallel orientations than for perpendicular orientations. The α for the random orientation was almost the same as that for the perpendicular orientation. Weak orientation dependence was observed in α for GlyH^+ and CH_4N^+ , while stronger orientation dependence was observed in that for NH_4^+ . For all secondary-ion species, the α for parallel orientation tended to be larger than that for perpendicular orientation. This implies that the vicinage effect for linear cluster projectiles is more pronounced for parallel orientation than for perpendicular orientation when comparing the same

cluster size. This trend agrees with our previous study [10] and also with the average number of secondary electrons emitted from carbon foil induced by 8-MeV He_2^+ impact [7]. Because α for fragments of CH_4N^+ and NH_4^+ were higher than that for intact ion of GlyH^+ , the fragmentation process seemed to be more sensitive to the incident cluster size than the ionization process. For small gold cluster impacts on phenylalanine (Phe) targets, the exponent for PheH^+ emission is reportedly 1.6 [33], which is comparable to the present results.

IV. DISCUSSION

We considered the dependence of secondary-ion yield on electronic stopping power. The electronic stopping power was calculated using linear-response dielectric theory [4,34,35]. The calculation method is described in the Appendix. Table I shows the calculated stopping power of glycine for C_n^+ ($n \leq 4$) with an energy of 0.9 MeV per atom and different structures and orientations.

To examine the validity of the calculations, we compared the present calculation for atomic carbon projectiles with that obtained from the SRIM code [36]. The present calculation ($55 \text{ eV } \text{\AA}^{-1}$) showed good agreement with the SRIM calculation ($56 \text{ eV } \text{\AA}^{-1}$). For the linear structures, the stopping power was obtained as an average for each orientation angle range (parallel: 0° – 30° , perpendicular: 60° – 90°). For linear projectiles, the stopping power for the perpendicular orientation was larger than that for the parallel orientation. This trend agreed with the energy-loss calculation of carbon-cluster ions in carbon foil [3]. For the ring-structured projectiles, the stopping power was higher than that for the linear projectiles both for $n = 3$ and 4. Interestingly, the stopping power for linear-parallel projectiles exhibited sublinear dependence [$S_e(n) < nS_e(1)$], while that for linear-perpendicular projectiles and ring-perpendicular projectiles exhibited superlinear dependence [$S_e(n) > nS_e(1)$]. Therefore, the incident cluster structure and orientation may affect the magnitude of the vicinage effect as well as the incident velocity [1].

We studied the correlation between the secondary-ion yield and stopping power. Figure 6 shows this relationship for clusters with various structures. The dependence of secondary-ion yield on the stopping power was significantly affected by the geometrical characteristics of the cluster projectiles. When considering the orientation effect of linear clusters at the same

TABLE I. Calculated electronic stopping power S_e of glycine for incident cluster ions C_n^+ ($n \leq 4$) with an energy of 0.9 MeV per atom and different cluster sizes n , structures, and orientations.

Cluster size	Structure	Orientation	S_e (eV \AA^{-1})
$n = 1$			55
$n = 2$	Linear	Parallel	90
		Perpendicular	119
$n = 3$	Linear	Parallel	115
		Perpendicular	185
	Ring	Perpendicular	183
$n = 4$	Linear	Parallel	140
		Perpendicular	251
		Ring	Perpendicular

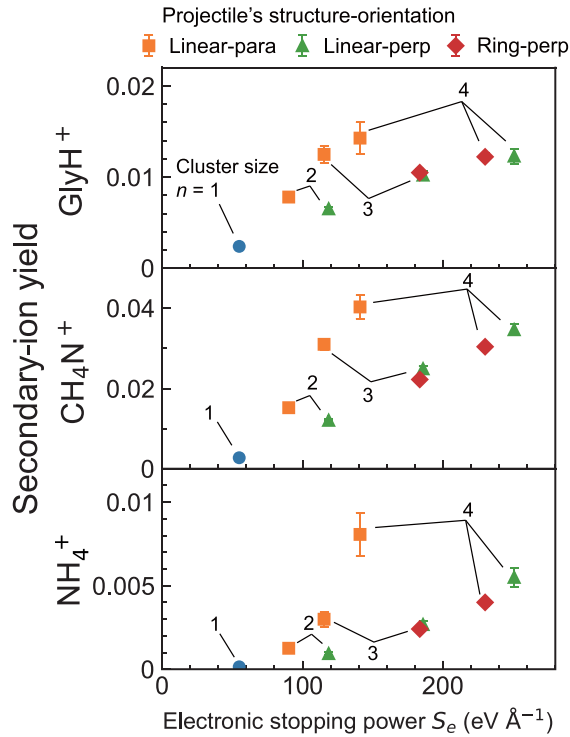


FIG. 6. Electronic stopping-power dependence of the secondary-ion yield for Gly-related positive secondary ions (GlyH⁺, CH₄N⁺, and NH₄⁺). The abscissa shows the calculated electronic stopping power of the glycine target for C_n⁺ projectiles, which was taken from Table I. The symbols show the geometrical structure type of the incident projectiles (orange squares: linear and parallel, green triangles: linear and perpendicular, red diamonds: ring and perpendicular).

electronic stopping power, projectiles in parallel orientations tended to produce more secondary ions than those in perpendicular orientations. It is known that the secondary-ion yield is scaled by the power law of electronic stopping power S_e^α in various models for the secondary-ion emission process induced by atomic ion impacts [37–39]. This means that the secondary-ion yield can be estimated when the electronic stopping power is given. However, that does not seem to be the case in cluster-ion impacts, where the structure and orientation of the cluster projectile play an important role.

The geometrical characteristics of cluster projectiles could affect both the stopping power and the cross-sectional area of the ion track A_t . Variation in the area of the ion track may change the deposited energy density and thus the secondary-ion yield. To examine this dependence, we estimated the energy density induced by cluster projectiles taking into consideration the cluster structure and orientation. Figure 7 shows a schematic of a model for estimating the energy density in the ion track induced by fast cluster projectiles with different structures and orientations, where r_t is the radius of the ion track produced by atomic projectiles and b_{ij} is the perpendicular component of the internuclear vector between the i th and j th atoms. The energy density is obtained by dividing the electronic stopping power S_e by the cross-sectional area of the ion track A_t . First, we estimated A_t of the ion-track region as a superposition of ion-track regions induced by each constituent ion. For comparison, the estimation was performed

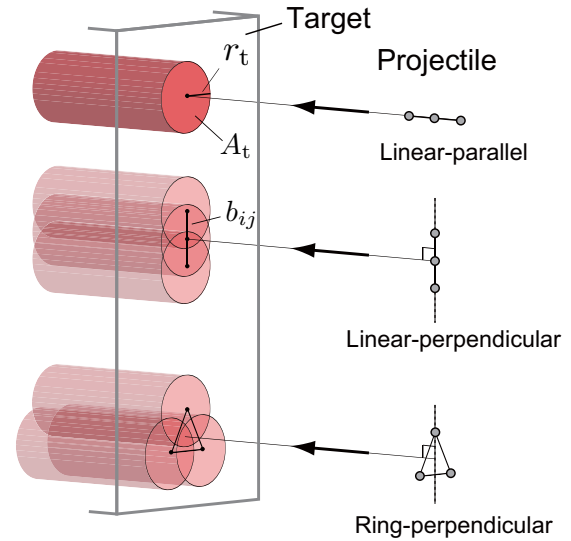


FIG. 7. A model of ion tracks considering cluster structure and orientation. r_t is the radius of the ion track induced by each constituent atom, and A_t is the cross-sectional area as a superposition of ion-track regions induced by each constituent ion. b_{ij} is the perpendicular component of the internuclear vector between the i th and j th atoms with respect to the beam direction.

for the infratrack and the ultratrack. The infratrack is the region where energy transfer occurs directly from the projectile to the electrons in the stopping medium. The radius of the infratrack r_{intra} is expressed as $r_{\text{intra}} \approx 6.7 \times (E/M)^{1/2}$ (Å), where E is the kinetic energy of the projectile in MeV and M is the mass of the projectile in atomic mass units [40]. The ultratrack is the region defined by the range of the most energetic secondary electrons (δ electrons) produced in the track core. The radius of the ultratrack is estimated as $r_{\text{ultra}} \approx 830 \times E / (\rho_{\text{Gly}} M)$ (Å) [40], where ρ_{Gly} is the density of glycine ($\rho_{\text{Gly}} = 1.16 \text{ g cm}^{-3}$). Under the present conditions ($E = 0.9 \text{ MeV}$, $M = 12 \text{ amu}$), r_{intra} and r_{ultra} were estimated at 1.83 and 53.7 Å, respectively. Table II shows the estimated cross-sectional area A_t for each cluster size and geometrical structure. Using these results, we obtained a deposited energy density of $0.5S_e/A_t$, where S_e is the calculated electronic stopping power listed in Table I. The factor of 0.5 originates from an equipartition rule stating the equality of energy deposited on the infratrack and that deposited on the ultratrack [41].

Figure 8 shows the secondary-ion yield of each secondary-ion species as a function of the deposited energy density in the infratrack region. Figure 8 shows a universal relationship between the secondary-ion yield and energy density regardless of the cluster size, orientation, and structure. Although we also investigated the dependence of the secondary-ion yield on the energy density in the ultratrack, there was no correlation between the energy density and secondary-ion yield. Therefore, we concluded that the deposited energy density in the infratrack region was a key parameter in the secondary-ion emission process induced by fast cluster-ion impacts. This result is well supported by a scenario proposed by Sundqvist [40], in which the emission of intact ions from biomolecular targets is caused by expansion of the track core. This finding may enable estimation of the electronic sputtering yield

TABLE II. Estimated area of the ion-track cross section of incident cluster ions for cluster ions C_n^+ ($n \leq 4$) with an energy of 0.9 MeV per atom and different cluster sizes n , structures, and orientations. The radii of infra- and ultratracks obtained from the model calculation were 1.83 and 53.7 Å, respectively.

Cluster size	Structure	Orientation	Infratrack (10^{-19} m^2)	Ultratrack (10^{-17} m^2)
$n = 1$			1.1	9.1
$n = 2$	Linear	Parallel	1.1	9.1
		Perpendicular	1.6	9.2
$n = 3$	Linear	Parallel	1.1	9.1
		Perpendicular	2.1	9.4
	Ring	Perpendicular	2.0	9.3
$n = 4$	Linear	Parallel	1.1	9.1
		Perpendicular	2.6	9.5
	Ring	Perpendicular	2.5	9.4

caused by larger cluster projectiles, including C_{60} ions with megaelectron volt energy, and is currently under investigation.

V. CONCLUSIONS

We investigated the effect of the structures and orientations of C_n^+ ($n \leq 4$) cluster projectiles on secondary-ion emission from thin foil. Coincidence measurements were performed for Coulomb explosion imaging of cluster projectiles and TOF mass spectrometry of secondary ions emitted in the forward direction from the target. Using cluster projectiles with linear and ring structures and parallel and perpendicular orientations, we investigated the yields of the Gly-related secondary ions GlyH^+ , CH_4N^+ , and NH_4^+ and obtained the following results:

(i) The secondary-ion yield for linear cluster projectiles in the orientation parallel to the beam direction tended to be larger than that for the other cases irrespective of the cluster size.

(ii) The stopping-power dependence of the secondary-ion yield showed different trends with cluster structure and orientation. This result suggests that the vicinage effect in secondary-ion emission arises from both the change in electronic stopping power and the change in other geometrical parameters such as the cross-sectional area of the ion-track region.

(iii) A universal relationship was found between the deposited energy density in the infratrack region and the secondary-ion yield, implying that the emission of molecular secondary ions from biomolecules arose from expansion of the track-core region.

(iv) This finding may help with understanding the electronic sputtering process caused by large cluster projectiles, including C_{60} ions with megaelectron volt energy, which is currently under investigation.

ACKNOWLEDGMENTS

We thank M. Naitoh and Y. Sasaki of Kyoto University for technical support during the experiments. This work was supported by the Kyoto University Foundation.

APPENDIX

We calculated the stopping power for swift cluster ions using a linear-response dielectric formalism [4,34,35]. This calculation is known to reproduce the experimental results well [1]. According to the dielectric formalism, the electronic stopping power S_e for charged particles with velocity \vec{v} is described as follows:

$$S_e = \frac{1}{2\pi^2} \frac{1}{v} \int d^3k \int d\omega \frac{i\vec{k} \cdot \vec{v} \delta(\omega - \vec{k} \cdot \vec{v})}{k^2 \varepsilon(k, \omega)} \times |\rho(\vec{k})|^2 \exp[i(\omega - \vec{k} \cdot \vec{v})t], \quad (\text{A1})$$

where k and ω are the momentum and the energy transferred to the target electrons, respectively; $\varepsilon(k, \omega)$ is the dielectric function for the stopping medium; and $\rho(\vec{k})$ is the charge density of projectiles taking into consideration the orientation

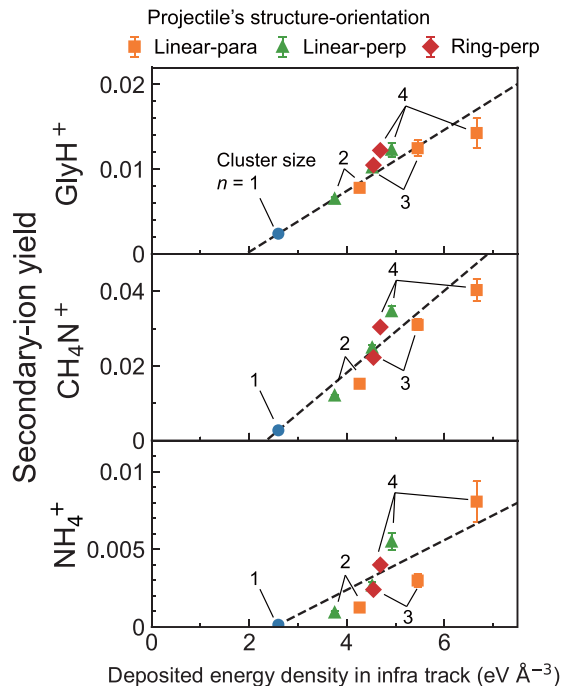


FIG. 8. Energy density dependence of secondary-ion yield for Gly-related positive secondary ions (GlyH^+ , CH_4N^+ , and NH_4^+). The abscissa shows the energy density deposited in the infratrack region. The lines are included as a visual guide.

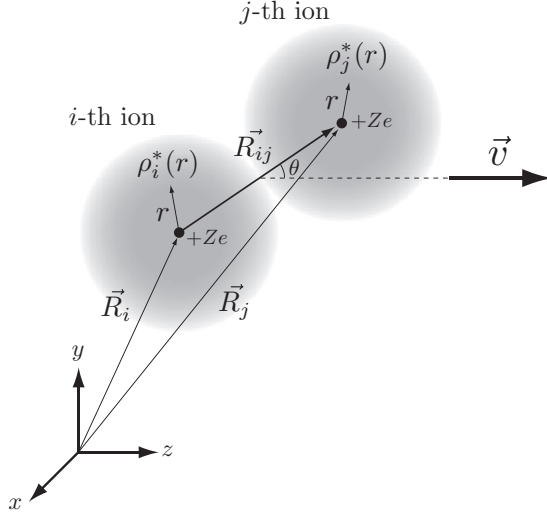


FIG. 9. A model of cluster constituent atoms used in the stopping-power calculation. A cluster projectile moved along the z axis with velocity v . Coordinates of the i th and the j th constituent atoms are represented on a two-dimensional grid. Each constituent ion consists of a nucleus and bound electron. \vec{R}_i and \vec{R}_j are position vectors of nuclei for the i th and j th constituent atoms, respectively. $\rho_i^*(r)$ is the charge density of the bound electrons of the i th ion, which is a function of the distance r from the nucleus of the i th ion. The magnitude of interference between two constituent atoms is characterized by the internuclear vector $\vec{R}_{ij} = \vec{R}_j - \vec{R}_i$ and the orientation angle θ with respect to the beam direction.

and structure of the cluster projectiles. Figure 9 shows a model of the cluster projectiles. The charge density $\rho(\vec{\chi})$ of a cluster ion consisting of n atoms can be expressed as the sum of the charge densities of individual atomic ions as follows:

$$\rho(\vec{\chi}) = \sum_i^n \rho_i(\vec{\chi} - \vec{R}_i), \quad (\text{A2})$$

where ρ_i and \vec{R}_i are the charge density and the position vector of the i th atomic ion, respectively. The charge density of an individual atomic ion has the following form:

$$\rho_i(\vec{\chi} - \vec{R}_i) = e[Z\delta(\vec{\chi} - \vec{R}_i) - \rho_i^*(\vec{\chi} - \vec{R}_i)], \quad (\text{A3})$$

where the first term is the nuclear charge and the second term, $\rho_i^*(\vec{\chi} - \vec{R}_i)$, is the charge density of the bound electrons. To describe the bound electrons, we used the Brandt-Kitagawa model [42]. In this model, the charge density of the bound electrons is described as follows:

$$\rho_i^*(r) = \frac{N_i}{4\pi\Lambda_i^3} \frac{\Lambda_i}{r} \exp(-r/\Lambda_i), \quad (\text{A4})$$

$$\Lambda_i = \frac{0.48\left(\frac{N_i}{Z}\right)^{\frac{2}{3}}}{Z^{\frac{1}{3}}\left[1 - \frac{1}{7}\frac{N_i}{Z}\right]} a_0, \quad (\text{A5})$$

where r is the distance from the nucleus, N_i is the number of bound electrons for the i th atomic ion, Λ_i is the screening length of the bound electrons, and a_0 is the Bohr radius. To obtain N_i , we treated individual atomic ions as partially stripped ions with an equilibrium average charge traversing a stopping medium. It is well known that the equilibrium

TABLE III. Combination of the number of bound electrons of individual atoms when the incident clusters of C_n^+ ($n \leq 4$), which have an energy of 0.9 MeV per atom and different structures, decomposed in matter.

Cluster size	Structure	Combination of bound electron numbers
$n = 1$		(4.0)
$n = 2$	Linear	(4.1, 4.1)
$n = 3$	Linear	(4.1, 4.2, 4.1)
	Ring	(4.2, 4.2, 4.2)
$n = 4$	Linear	(4.2, 4.2, 4.2, 4.2)
	Ring	(4.2, 4.2, 4.2, 4.2)

average charge of fast cluster ions in a solid tends to be lower than that of atomic ions with the same velocity [13]. We calculated the number of bound electrons for each constituent ion using a self-consistent calculation formalism proposed by Kaneko *et al.* [16]. The calculated numbers of bound electrons are shown in Table III for different cluster sizes and structures. The number of bound electrons changed for each constituent ion because the position effect in the charge state [12,14] was taken into consideration. To calculate the stopping power, we obtained the charge densities of the projectiles in Fourier space $\rho(\vec{k})$. For a cluster projectile with size n , $\rho(\vec{k})$ can be readily obtained from Eq. (A2) as follows:

$$\rho(\vec{k}) = \sum_i^n \rho_i(\vec{k}) \cdot \exp(-i\vec{k} \cdot \vec{R}_i), \quad (\text{A6})$$

where $\rho_i(\vec{k})$ is the charge density of the i th ion in Fourier space and is expressed as follows:

$$\rho_i(\vec{k}) = e[Z - \rho_i^*(\vec{k})], \quad (\text{A7})$$

where $\rho_i^*(\vec{k})$ is the charge density of bound electrons in Fourier space. For the Brandt-Kitagawa model distribution, $\rho_i^*(\vec{k})$ was obtained from Eq. (A4) as follows:

$$\rho_i^*(k) = \frac{N_i}{1 + (k\Lambda_i)^2}. \quad (\text{A8})$$

Substituting Eqs. (A6), (A7), and (A8) into Eq. (A1) gave an equation to calculate the stopping power for C_n^+ with $n = 2-4$:

$$S_e = S_A + S_B, \quad (\text{A9})$$

$$S_A = \frac{2}{\pi v^2} \int_0^\infty \frac{dk}{k} \int_0^{kv} d\omega \omega \times \sum_i^n \rho_i^2(k) \text{Im} \left[-\frac{1}{\varepsilon(k, \omega)} \right], \quad (\text{A10})$$

$$S_B = \frac{2}{\pi v^2} \int_0^\infty \frac{dk}{k} \int_0^{kv} d\omega \omega \times \sum_i^n \sum_{j, i \neq j}^n \rho_i(k) \rho_j(k) J_0 \left[b_{ij} \sqrt{k^2 - \left(\frac{\omega}{v}\right)^2} \right] \times \cos \left(\frac{\omega d_{ij}}{v} \right) \text{Im} \left[-\frac{1}{\varepsilon(k, \omega)} \right], \quad (\text{A11})$$

TABLE IV. Estimated average internuclear distances between cluster constituent atoms in matter. The initial internuclear distances for different cluster sizes and structures were taken from the *ab initio* calculations [17,22,23].

Cluster size	Structure	R_{ij} (Å)
$n = 2$	Linear	(1.5)
$n = 3$	Linear	(1.4, 1.4)
	Ring	(1.6, 1.6, 1.7)
$n = 4$	Linear	(1.4, 1.3, 1.4)
	Ring	(1.6, 1.6, 1.6, 2.0, 2.6)

where S_A is the energy loss of each ion as an independent ion and S_B is the additional energy loss caused by interference because of simultaneous excitation of the target by correlated ions. $J_0(\dots)$ is the zero-order Bessel function of the first kind. The parameters d_{ij} and b_{ij} are the parallel and perpendicular components of the internuclear vector, which were calculated as $d_{ij} = |\vec{R}_{ij}| \cos \theta$ and $b_{ij} = |\vec{R}_{ij}| \sin \theta$. Here, $\vec{R}_{ij} = \vec{R}_j - \vec{R}_i$ is the internuclear vector between the i th and j th constituents determined by the geometrical structure of the cluster projectiles, and θ is the orientation angle of the internuclear vector with respect to the beam direction. We assumed the initial geometrical structures of the cluster projectiles were linear or ring structures, which were computed with *ab initio* calculations [17,22,23]. During foil transmission of cluster projectiles, internuclear distances $R_{ij} = |\vec{R}_{ij}|$ increased because of Coulomb repulsion. We estimated the increment of R_{ij} during the foil transmission by solving Newton's equation of motion for individual cluster constituents. A screened Coulomb potential was chosen for the interaction potential [2]. The thickness of the target foil was assumed to be 13 nm. Under the present conditions, the increment of the internuclear distances after foil transmission was small (estimated to be less than 30%) because of the thinness of the target foil. Thus, for calculation of the stopping power, we used the average

internuclear distances, which were obtained as averages of the internuclear distances at the foil entrance and those at the foil exit. R_{ij} used for the calculation of the stopping power are shown in Table IV. For a linear structure, R_{ij} are indicated in the order of arrangement of each atomic ion. For a ring structure, R_{ij} for all combinations are indicated. $\text{Im}[-1/\varepsilon(k, \omega)]$ is the energy-loss function (ELF) of the target, which describes its response to an external perturbation. For calculation of the ELF $\text{Im}[-1/\varepsilon(k, \omega)]$, we applied the optical data model developed by Ashley [43]. In this model, the ELF is connected to the optical ELF (OELF) $\text{Im}[-1/\varepsilon(k=0, \omega)]$ as follows:

$$\omega \text{Im} \left[\frac{-1}{\varepsilon(k, \omega)} \right] = \int_0^\infty d\omega' \omega' \text{Im} \left[\frac{-1}{\varepsilon(0, \omega')} \right] \times \delta \left[\omega - \left(\omega' + \frac{\hbar k^2}{2m_e} \right) \right]. \quad (\text{A12})$$

The OELF of glycine is obtained from an empirical approach proposed by Tan *et al.* [44], which is expressed as follows:

$$\text{Im} \left[\frac{-1}{\varepsilon(0, \omega)} \right] = \frac{a(\hbar\omega)}{[(\hbar\omega)^2 - b^2]^2 + c^2(\hbar\omega)^2}, \quad (\text{A13})$$

with $b = 19.927 + 0.9807\bar{Z}$, $c = 13.741 + 0.3215\bar{Z}$ (eV). \bar{Z} is the mean atomic number of glycine ($\bar{Z} = 4.0$), and a is a parameter that is determined by the f -sum rule of the OELF:

$$\int_0^\infty d\omega \omega \text{Im} \left[\frac{-1}{\varepsilon(0, \omega)} \right] = \frac{\pi}{2} \omega_p^2, \quad \omega_p = \left(\frac{4\pi n_e e^2}{m_e} \right)^{\frac{1}{2}}, \quad (\text{A14})$$

where ω_p is the plasma frequency and n_e is the number density of electrons that contribute to the stopping power. We assumed n_e was the number density of valence electrons because inner-shell excitation does not contribute in this case with the low beam velocity. We readily confirmed that the f -sum rule was obeyed for all k if the OELF ($k=0$) obeyed Eq. (A14).

- [1] S. Tomita, M. Murakami, N. Sakamoto, S. Ishii, K. Sasa, T. Kaneko, and H. Kudo, Reduction in the energy loss of 0.5-MeV-per-atom carbon-cluster ions in thin carbon foils, *Phys. Rev. A* **82**, 044901 (2010).
- [2] S. Heredia-Avalos and R. Garcia-Molina, Reduction of the energy loss of swift molecular ions in solids due to vicinage effects in the charge state, *Phys. Rev. A* **76**, 032902 (2007).
- [3] T. Kaneko, Sublinear and superlinear dependences of average charge and energy loss per ion on particle number for MeV/atom linear-chained carbon-cluster ions traversing a carbon foil, *Phys. Rev. A* **86**, 012901 (2012).
- [4] R. Garcia-Molina, S. Heredia-Avalos, and I. Abril, Molecular structure effects in the energy loss of swift boron molecular ions in solids, *J. Phys.: Condens. Matter* **12**, 5519 (2000).
- [5] H. Rothard, K. Kroneberger, E. Veje, A. Clouvas, J. Kemmler, P. Koschar, N. Keller, S. Lencinas, P. Lorenzen, O. Heil, D. Hofmann, and K. O. Groeneveld, Experimental study of molecular and cluster effects in secondary electron emission, *Phys. Rev. B* **41**, 3959 (1990).
- [6] S. Tomita, Y. Shiina, S. Tamura, R. Kinoshita, S. Ishii, and K. Sasa, Measurement of backward secondary-electron yield under molecular ion impact coincident with emerging projectiles, *Nucl. Instrum. Methods Phys. Res. Sect. B* **354**, 109 (2015).
- [7] T. Azuma, Y. Yamazaki, K. Komaki, M. Sekiguchi, T. Hasegawa, T. Hattori, and K. Kuroki, Secondary electron emission from a C-foil resulting from the passage of orientation selected He_2^+ molecular ions, *Nucl. Instrum. Methods Phys. Res. Sect. B* **67**, 636 (1992).
- [8] H. H. Andersen, A. Brunelle, S. Della-Negra, J. Depauw, D. Jacquet, Y. Le Beyec, J. Chaumont, and H. Bernas, Giant Metal Sputtering Yields Induced By 20–5000 keV/atom Gold Clusters, *Phys. Rev. Lett.* **80**, 5433 (1998).
- [9] Y. Le Beyec, Cluster impacts at keV and MeV energies: Secondary emission phenomena, *Int. J. Mass Spectrom. Ion Processes* **174**, 101 (1998).
- [10] R. Murase, H. Tsuchida, S. Tomita, A. Chiba, K. Nakajima, T. Majima, and M. Saito, Effects of molecular axis orientation of MeV diatomic projectiles on secondary ion emission from

- biomolecular targets, *Nucl. Instrum. Methods Phys. Res. Sect. B* **478**, 284 (2020).
- [11] H. Tsuchida, N. Nitta, Y. Yanagida, Y. Okumura, and R. Murase, Fibrous structure in GaSb surfaces irradiated with fast Cu cluster ions, *J. Appl. Phys.* **123**, 161548 (2018).
- [12] T. Kaneko, Theory of average charge and energy loss of cluster ions in foils, *Phys. Rev. A* **66**, 052901 (2002).
- [13] A. Brunelle, S. Della-Negra, J. Depauw, D. Jacquet, Y. Le Beyec, and M. Pautrat, Reduced charge state of MeV carbon cluster constituents exiting thin carbon foils, *Phys. Rev. A* **59**, 4456 (1999).
- [14] A. Chiba, Y. Saitoh, K. Narumi, M. Adachi, and T. Kaneko, Average charge and its structure dependence of fragment ions under irradiation of a thin carbon foil with a 1-MeV/atom C_3^+ cluster ion, *Phys. Rev. A* **76**, 063201 (2007).
- [15] M. F. Steuer, D. S. Gemmell, E. P. Kanter, E. A. Johnson, and B. J. Zabransky, Diminished stopping power for fast nitrogen and oxygen diclusters in carbon, *Nucl. Instrum. Methods Phys. Res.* **194**, 277 (1982).
- [16] T. Kaneko, K. Ihara, and M. Kohno, Electronic stopping for swift carbon cluster ions connected with average charge reduction, *Nucl. Instrum. Methods Phys. Res. Sect. B* **315**, 76 (2013).
- [17] C. Petrongolo, P. J. Bruna, S. D. Peyerimhoff, and R. J. Buenker, Theoretical prediction of the potential curves for the lowest-lying states of the C_2^+ molecular ion, *J. Chem. Phys.* **74**, 4594 (1981).
- [18] A. Van Orden and R. J. Saykally, Small carbon clusters: Spectroscopy, structure, and energetics, *Chem. Rev.* **98**, 2313 (1998).
- [19] G. Von Helden, M. T. Hsu, N. Gotts, and M. T. Bowers, Carbon cluster cations with up to 84 atoms: Structures, formation mechanism, and reactivity, *J. Phys. Chem.* **97**, 8182 (1993).
- [20] A. Faibis, E. P. Kanter, L. M. Tack, E. Bakke, and B. J. Zabransky, Geometrical structure of C_3^+ , *J. Phys. Chem.* **91**, 6445 (1987).
- [21] Z. Vager and E. P. Kanter, An alternative interpretation of Coulomb explosion data on C_3^+ , *J. Phys. Chem.* **93**, 7745 (1989).
- [22] Z. D. Wang and P. A. Withey, Comprehensive survey of the structures of C_4 , C_4^- , and C_4^+ clusters, *Chem. Select* **3**, 13355 (2018).
- [23] A. Fura, F. Tureček, and F. W. McLafferty, Small carbon clusters (C_n^0 , C_n^+ , C_n^-) from acyclic and cyclic precursors: Neutralization-reionization and theory, *Int. J. Mass Spectrom.* **217**, 81 (2002).
- [24] A. Benninghoven, D. Jaspers, and W. Sichtermann, Secondary-ion emission of amino acid, *Appl. Phys.* **11**, 35 (1976).
- [25] M. Suzuki, M. Nojima, M. Fujii, T. Seki, and J. Matsuo, Mass analysis by Ar-GCIB-dynamic SIMS for organic materials, *Surf. Interface Anal.* **46**, 1212 (2014).
- [26] M. Kawecki and L. Bernard, Database of proteinogenic amino acid reference spectra for bismuth-cluster ToF-SIMS. II. Positive polarity, *Surf. Sci. Spectra* **25**, 015002 (2018).
- [27] I. M. Weiss, C. Muth, R. Drumm, and H. O. Kirchner, Thermal decomposition of the amino acids glycine, cysteine, aspartic acid, asparagine, glutamic acid, glutamine, arginine and histidine, *BMC Biophys.* **11**, 2 (2018).
- [28] Z. Vager, R. Naaman, and E. P. Kanter, Coulomb explosion imaging of small molecules, *Science* **244**, 426 (1989).
- [29] E. R. Amstalden van Hove, D. F. Smith, and R. M. Heeren, A concise review of mass spectrometry imaging, *J. Chromatogr. A* **1217**, 3946 (2010).
- [30] M. Adachi, Y. Saitoh, A. Chiba, K. Narumi, K. Yamada, and T. Kaneko, Monte Carlo particle trajectory simulation for classification of C_3^+ cluster ion structure utilizing Coulomb explosion imaging, *Radiat. Phys. Chem.* **77**, 1328 (2008).
- [31] D. Kella, M. Algranati, H. Feldman, O. Heber, H. Kovner, E. Malkin, E. Miklazky, R. Naaman, D. Zajfman, J. Zajfman, and Z. Vager, A system for Coulomb explosion imaging of small molecules at the Weizmann Institute, *Nucl. Instrum. Methods Phys. Res. Sect. A* **329**, 440 (1993).
- [32] X. Dong, A. Gusev, and D. M. Hercules, Characterization of polysiloxanes with different functional groups by time-of-flight secondary ion mass spectrometry, *J. Am. Soc. Mass Spectrom.* **9**, 292 (1998).
- [33] K. Boussofiane-Baudin, A. Brunelle, P. Chaurand, S. Della-Negra, J. Depauw, P. Håkansson, and Y. Le Beyec, Non-linear sputtering effects induced by MeV energy gold clusters, *Nucl. Instrum. Methods Phys. Res. Sect. B* **88**, 61 (1994).
- [34] W. Brandt, A. Ratkowski, and R. H. Ritchie, Energy Loss of Swift Proton Clusters in Solids, *Phys. Rev. Lett.* **33**, 1325 (1974).
- [35] N. R. Arista, Energy loss of correlated charges in an electron gas, *Phys. Rev. B* **18**, 1 (1978).
- [36] J. F. Ziegler, M. D. Ziegler, and J. P. Biersack, SRIM - The stopping and range of ions in matter (2010), *Nucl. Instrum. Methods Phys. Res. Sect. B* **268**, 1818 (2010).
- [37] K. Kitajima, H. Tsuchida, T. Majima, and M. Saito, Effects of electronic stopping power on fast-ion-induced secondary ion emission from methanol microdroplets, *Eur. Phys. J. D* **72**, 169 (2018).
- [38] R. E. Johnson, B. U. Sundqvist, A. Hedin, and D. Fenyö, Sputtering by fast ions based on a sum of impulses, *Phys. Rev. B* **40**, 49 (1989).
- [39] R. E. Johnson, Mechanisms for the desorption of large organic molecules, *Int. J. Mass Spectrom. Ion Process.* **78**, 357 (1987).
- [40] B. U. R. Sundqvist, Ion track structure probed by plasma desorption mass spectrometry, *Int. J. Mass Spectrom. Ion Process.* **126**, 1 (1993).
- [41] A. Hedin, P. Håkansson, B. Sundqvist, and R. E. Johnson, Ion-track model for fast-ion-induced desorption of molecules, *Phys. Rev. B* **31**, 1780 (1985).
- [42] W. Brandt and M. Kitagawa, Effective stopping-power charges of swift ions in condensed matter, *Phys. Rev. B* **25**, 5631 (1982).
- [43] J. C. Ashley, Optical-data model for the stopping power of condensed matter for protons and antiprotons, *J. Phys.: Condens. Matter* **3**, 2741 (1991).
- [44] Z. Tan, Y. Xia, M. Zhao, and X. Liu, Electron stopping power and inelastic mean free path in amino acids and protein over the energy range of 20–20,000 eV, *Radiat. Environ. Biophys.* **45**, 135 (2006).